Geophysical Journal International

Geophys. J. Int. (2019) **219,** 449–463
Advance Access publication 2019 July 11
GJI Seismology

doi: 10.1093/gji/ggz297

Seismic activity during the 2013–2015 intereruptive phase at Lascar volcano, Chile

Ayleen Gaete ,[1] Simone Cesca,[1] Luis Franco,[2] Juan San Martin,[3] Cristian Cartes[3] and Thomas R. Walter[1]

[1] *GFZ German Research Centre for Geosciences, Telegrafenberg, 14473 Potsdam, Germany. E-mail: agaete@gfz-potsdam.de*
[2] *Observatorio Volcanológico de Los Andes del Sur (OVDAS), Servicio Nacional de Geología y Minería (SERNAGEOMIN), Temuco, Chile*
[3] *Physics Science Department, Universidad de la Frontera, Casilla 54-D, Temuco, Chile*

Accepted 2019 June 29. Received 2019 May 21; in original form 2019 January 25

SUMMARY

In addition to enabling the physical processes of volcanic systems to be better understood, seismology has been also used to infer the complexity of magma pathways and plumbing systems in steep-sided andesitic and stratovolcanoes. However, in these volcanic environments, the application of seismic location methods is particularly challenging and systematic comparisons of common methods are lacking. Furthermore, little is known about the characteristic seismicity and deep structure of Lascar volcano, one of the most historically active volcanoes in northern Chile known to produce VEI-4 eruptions. To better understand the inner processes and deep structure of Lascar, the local broad-band seismic monitoring network was densified during a temporal installation in 2014–2015. Herein, we focus on the local seismicity during the 2014–2015 unrest episode, during which we recorded numerous seismic events mainly classified as long-period (LP) type, but also denote volcano-tectonic (VT) activity. Specifically, a long-lasting phase of LP activity is observed over a period of ∼14 months that starts in tandem with a pulse of VT activity. The LP rate and amplitude are modulated over time; they are lower in the initial phase, rise during the intermediate period from October 2014 to July 2015, and finally slowly decay while approaching the eruption time. The location of LPs is challenging due to the typical lack of clear seismic onsets. We thus encompass this problem by comparing a broad range of different standard and novel location techniques to map the source region of LPs by fitting the amplitude decay, polarization patterns, coherence of characteristic functions and cross-correlation differential times. As a result, we principally constrain LP locations within the first 5 km depth below the summit extending downward along a narrow, conduit-like path. We identify different regions of complexity: VTs dominate at depth, both VTs and LPs cluster in an intermediate depth region (down to 1.5 km), suggesting a change in the plumbing system geometry, and LPs dominate the shallowest region. Based on these results, we infer the presence of a subvertical conduit extending down to a depth of ∼5 km, and a region of path divergence, possibly accommodating a magma plumbing system, at a depth of ∼3 km beneath the volcano summit. Identifying the locations of complexities in the magma pathways at Lascar may help identify future unrest. The results are compared with independent observations, demonstrating the strength of the location method used herein that will be tested at volcanoes elsewhere.

Key words: South America; Magma chamber processes; Volcano monitoring; Volcano seismology.

1 INTRODUCTION

Volcanic eruptions are fed by magma, which is stored within and transported through plumbing systems formed by extensive networks of reservoirs and conduits beneath volcanoes. The physical processes that produce eruptions and their associated dynamics can be better understood by studying these plumbing systems from multiple perspectives through a variety of disciplines, including geology and structural analysis, petrology and geochemistry, geophysics and geodesy and modelling (Burchardt & Galland 2016). In particular, some volcanoes, especially basaltic ones, often display clear internal structures featuring dikes, rift zones and magma chambers (Dzurisin 2007), whereas the characteristics of explosive and often dome-building volcanoes are difficult to reconcile due to the absence of major storage regions and/or scattering effects observed in geophysical data (Wegler & Lühr 2001).

Seismology is a common geophysical discipline through which active volcanoes are monitored and studied, usually by examining processes associated with the stationary and/or transport effects of magma and gas that produce resonance and brittle earthquake sources, as their spatiotemporal migration and focal mechanisms and can provide insight to volcanic structure. A large variety of seismic signals are typically recorded in volcanic environments in response to source mechanisms and are classified by their waveform and spectral characteristics (e.g. Chouet 2003; Kawakatsu & Yamamoto 2015; Nakano & Kumagai 2005). Volcano-tectonic (VT) signals, the features of which resemble those of tectonic earthquake waveforms, such as clear, high-frequency P and S onsets, are interpreted to be related to brittle failures, possibly as a consequence of magma migration and stress perturbations (Wassermann 2012). In contrast, long-period (LP) seismic signals, which are typically observed at volcanoes, are characterized by emergent onsets, the lack of a clear S phase, a narrow band or monochromatic radiation and a predominantly low-frequency content of 0.2–10 Hz; LP signals have often been directly associated with shallow processes affecting volcanic plumbing systems (Del Pezzo *et al.* 2013). The production of these LP signals has been explained in two main ways: (1) LPs have been linked to resonance phenomena in response to gas and magma migration and pressure transients within low-viscosity fluid–gas mixtures, the sources of which have been successfully modelled by the resonance of fluid-filled fracture systems, cracks and conduits (Chouet, 1986, 1988; Neuberg *et al.* 2006); (2) LPs have also been explained as signals produced by slow-rupture failure in unconsolidated volcanic materials, resulting from the deformation of the shallow part of a volcanic edifice, thereby defining this source as a dry mechanism (Bean *et al.* 2014). In addition to VT and LP signals, a broader variety of seismic signals in volcanic environments have been proposed, including very-long period (VLP), volcanic tremor (TR), hybrid (HB) and explosion (EX) signals (Wassermann 2012). Nevertheless, the locations of VTs and LPs have been used to infer the geometries of plumbing systems. For instance, the lateral propagation of a ring dyke beneath Mammoth Mountain, USA, was depicted by the clockwise migration of a VT swarm over a period spanning less than 1 yr. In addition, deeper events clearly imaged along a near-vertical plane were interpreted as an intruding dyke (Prejean *et al.* 2003). Similarly, the locations of LP and tremor sources enabled the geometry of the shallow conduit that fed the eruption episodes at Mt. Etna in September and November 2007 to be constrained (Patanè *et al.* 2008); furthermore, the locations of sustained LP signals associated with hydrothermal activity were employed to define the extent of the source, which was verified with a resonance model consisting of a crack filled with a water-gas fluid in Campi Flegrei, Italy (Cusano *et al.* 2008).

Very active volcanoes located near to populated areas usually own permanent seismic network to monitor and record data in real time, thereby allowing the risk of volcanic eruption to be studied and assessed continuously. One of the most active volcanoes in the Andean central volcanic zone is Lascar (Fig. 1). This volcano (5592 m; 23°22′S, 67°44′W) is located at the southwestern part of the Altiplano-Puna Volcanic Complex (APVC; 21° to 24°S) which is characterized by a volcanism mainly andesitic laying on a 80-km-thick crust (Kay & Coira 2009). The formation of the APVC is associated with uplift produced by shortening of the crust due to plate convergence, a limited rate of magmatism due to shallow subduction processes, and an extensive and Tertiary ignimbrite responsible for producing the silicic volcanism in the region (de Silva 1989). Lascar is an andesitic volcano composed of two partially overlapping stratocones with five nested craters aligned in an ENE–WSW trend; three craters are located on the eastern stratocone, and two are located on the western stratocone. The westernmost crater, which is usually characterized by permanent degassing from a fumarole field associated with a magmatic–hydrothermal system (Tassi *et al.* 2009), located on the eastern edifice is the only currently active crater (Matthews *et al.* 1997). The magma chamber has been hypothesized to be as deep as 10–17 km beneath the volcano (González *et al.* 2015).

The historic record of activity contains two major eruptions that occurred in 1933 and 1993 (Global Volcanism Program 2013). The 1993 eruption with a Volcanic Explosivity Index (VEI) of 4 seemingly changed the geometry of both the active crater and the subvolcanic plumbing system (Matthews *et al.* 1997) and modified the normal volcano activity, as was discerned from the corresponding variation in infrared radiance (Wooster 2001). More than 10 eruptions have occurred in the 25 yr since 1993, including the two more recent events in April 2013 (VEI 1) and October 2015 (VEI 2) (Global Volcanism Program 2013). These two most recent eruptions were relatively short with a duration of approximately 1 hr; their eruptive style was characterized by post-incandescence and single explosive eruptions with a gas plume varying from white to grey with ash emissions that rose 320 and 2500 m for the 2013 and 2015 events, respectively, as reported by Observatorio Volcanologico de los Andes del Sur (OVDAS 2013, 2015). Both eruptions were effectively monitored by a permanent multiparametric monitoring network operational since the end of 2010 consisting of seismic stations, time-lapse cameras, differential optical absorption spectroscopy (DOAS) gas sampling instrument, weather stations, and temperature and multigas sensors.

Recent research on Lascar has incorporated a wide range of observations. The search for a shallow magma plumbing system motivated various satellite interferometric synthetic aperture radar (InSAR) studies (Pritchard & Simons 2002; Pavez *et al.* 2006), but interferometry was unable to reveal significant deformation associated with common phreatic eruptions. Local deformation was associated with the postdepositional contraction of material on the slopes (InSAR and GPR data; Whelley *et al.* 2012) and inside the craters (very high resolution (VHR) panchromatic and SAR data; Richter *et al.* 2018). In addition, numerous works have investigated the mechanism of crater formation. The development and continuous deepening of the Lascar craters is commonly explained by degassing within a shallow conduit system (Matthews *et al.* 1997) rather than by processes related to eruption. Active degassing from inside the craters, which has also been identified by remote sensing techniques (Bredemeyer *et al.* 2018), signifies the significant influence of a hydrothermal system, as is reflected by the ascension of deep fluids (Tassi *et al.* 2009). This can be attributed to the movement of fluid from a magma chamber at depths of 10–17 km as was realized by spectral radiance sensing that produced thermal variations during the observed period of 2000–2004 (González *et al.* 2015). At present, degassing and changes in the crater morphology continue to be observed; for example, terrestrial laser scanning exposed fresh structures (de Zeeuw-van Dalfsen *et al.* 2017) displaying gradients in high-resolution surface deformation maps (Richter *et al.* 2018). These high-resolution data suggest that the deformation of the eastern craters is related to gravitational

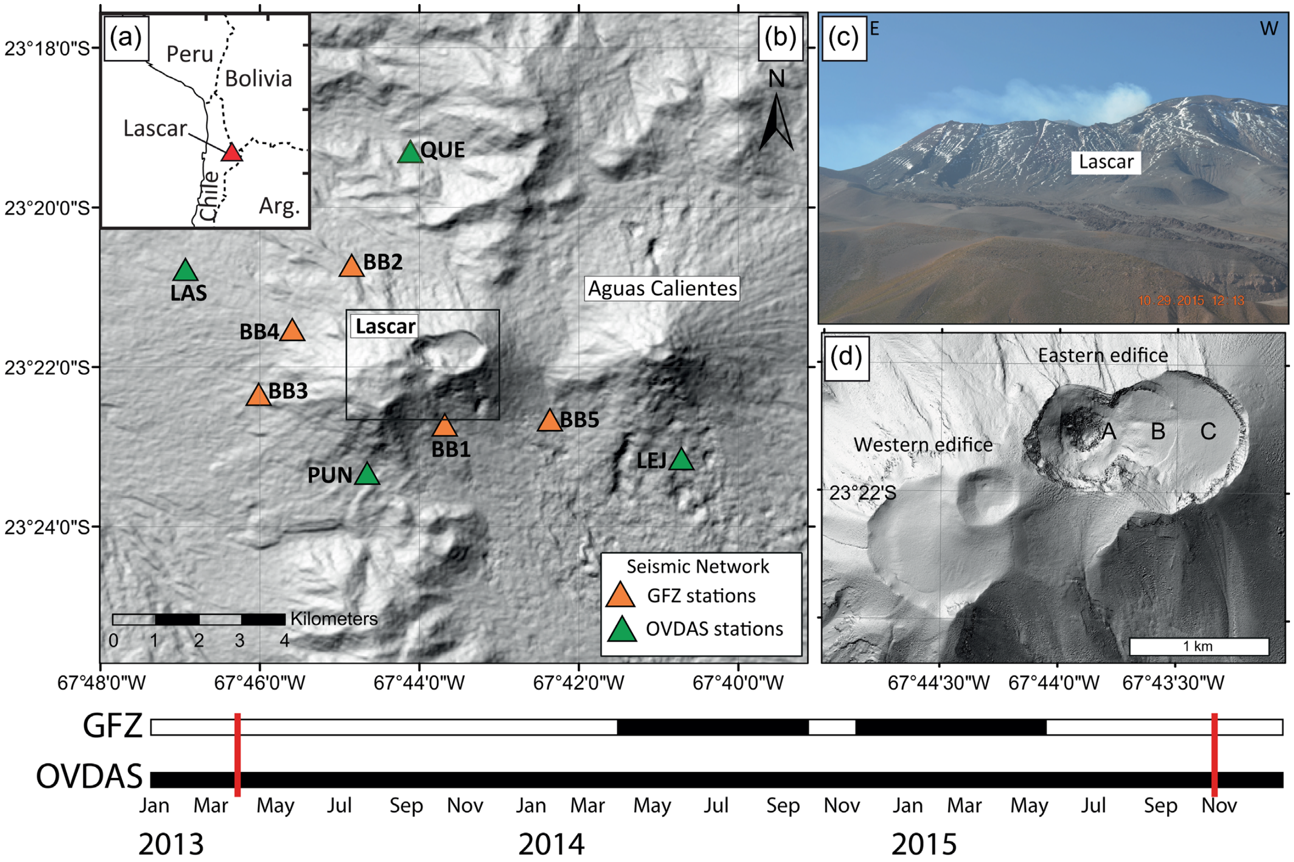

Figure 1. (a) Location of the study area. (b) Map of the area and seismic network deployed for monitoring Lascar volcano. (c) View of the northern flank of the active eastern edifice. (d) Amplified map of the inactive craters belonging to the western edifice and the eastern edifice with the nested active craters. The timelines show the operational durations of the OVDAS and GFZ seismic networks during the period covered by this study, during which Lascar produced two eruptions in 2013 and 2015 (red lines).

slumping, cooling, and the compaction of eruption products; however, these data do not provide evidence for deformation associated with a deeper plumbing system, magma pathway or magma chamber.

Some information is available about the deeper structure of Lascar. A seismological investigation identified long-term stationary harmonic tremors 1 yr after the 1993 eruption, but these signals were thought to be associated with fumarole degassing (Asch *et al.* 1996). Closer analysis of the source of this tremor indicated that it could be related to water and/or gas migration in a shallow hydrothermal system, possibly at a depth of 2–3 km (Hellweg 2000). Additionally, a magnetotelluric study (Díaz *et al.* 2012) imaged a high-conductivity volume at only ∼1 km beneath the summit, suggesting the presence of a shallow hydrothermal system; Díaz *et al.* (2012) further identified an anomaly at a depth of 6 km, which could be associated with a magma storage zone. Seismic wave interferometry allowed some scholars to speculate on the seismic velocity variations associated with inflation/deflation processes in a magmatic or hydrothermal reservoir during the period of unrest preceding the 2013 eruption (González *et al.* 2016). This velocity variation also coincided with an increase in the number of LPs, an intensification of fumarole degassing, and the phenomenon of crater incandescence. Similar changes were observed in the more recent 2015 episode of unrest, culminating in a short volcanic explosion on 30 October 2015 (Global Volcanism Program 2016).

Here, we provide a comprehensive analysis of the data acquired by broad-band seismic stations from both a permanent network and a temporary network (Fig. 1b) and focus on the locations of LPs and VTs, which represent the vast majority of signals recorded at Lascar during the 2013–2015 intereruptive phase. We take advantage of a dense seismological network and combine signal classification with source location and source characterization to analyse the various types of events, thereby allowing us to characterize the plumbing system beneath Lascar volcano and infer further constraints on possible fluid and magma ascent paths. Moreover, to account for the weak signal amplitudes, emergent signal onsets and poor signal-to-noise ratios of the LP sources, we compare different techniques that are commonly used for challenging event location tasks considering patterns of the signal amplitude, polarization, coherency and correlation. Finally, a joint seismological analysis is performed to propose a plausible model for the internal structure of Lascar.

2 METHODS

We investigate data acquired by both permanent and temporary networks. The permanent seismic network was installed in December 2012 by OVDAS and consist of 5 broad-band stations (LAS, QUE, LEJ, PUN and TAL) with a sampling rate of 100 Hz buried at a maximum height of 1 m above the bedrock. The temporal network operated from April 2014 to May 2015 with 5 additional broad-band stations (BB1, BB2, BB3, BB4, and BB5) at a 100 Hz sampling rate (Fig. 1). All seismometers were buried ∼1 m deep, thermally isolated and powered by battery/solar panels. The data were investigated using the standard classification (see section 2.1), and the location of LPs were evaluated using four different methods as described below. The full waveform data of the temporal network can be openly accessed through the GEOFON (1993) data archive (https://geofon.gfz-potsdam.de/).

2.1 Signal characterization

Seismic data from the permanently operating OVDAS network are routinely scanned to detect and classify local seismic signals at Lascar, and event detection is performed in real time through visual inspection and classification. Event classification is based on the spectral content, harmonic signature and duration of the waveforms (Latter 1981, Lahr *et al.* 1994, Chouet 1996, Chouet & Matoza 2013); as a result, the seismic activity at Lascar can be classified into volcanic-tectonic (VT), long-period (LP), very long-period (VLP), volcanic tremor (TR), hybrid (HB) or explosion (EX) signals.

The OVDAS seismic catalog contains 2893 events in the time period from 1 January 2013 to 25 December 2015, covering the whole inter-eruption phase from April 2013 to October 2015. From this catalog, we considered two types of events, VT and LP events, which are the most abundant and cover more than 85 per cent of the original catalog (approximately 2000 LPs and 350 VTs). The remaining 15 per cent of the catalog corresponds to the other signals listed above (HB, EX and TR signals). LP and VT signals recorded at Lascar (see examples in Figs 2a and b) present typical spectral contents and P phase properties similar to those observed at other volcanoes (e.g. Chouet 1996). The LP spectra (Fig. 2a) are restricted to the frequency band between 0.2 and 10 Hz, show an emergent phase onset and lack clear *P* and *S* phases (McNutt 2005). On the other hand, the VT spectral content mostly exceeds 5 Hz and presents impulsive *P* and *S* phases (Fig. 2b).

The following methods concentrate principally on further analysing the identified LP events and their association with VT activity. The LP waveforms were visualized, and their first onsets were picked. While this picking procedure is not very accurate, given the emergent onset of LP signals, this approach is useful for automatically selecting time windows for the LP signals, which are used hereafter to perform signal polarization and cross-correlation analysis.

2.2 LP waveform similarity

We evaluate the similarity among the LP waveforms to search for different clusters and to assess their spatial and temporal variations. The concept of waveform similarity based on the cross-correlation of signals at one or multiple stations is an accepted method in volcanic environments for the automated classification and identification of seismic signals and for the amplitude estimation and recurrence analysis of different families of signals, specifically LP signals (e.g. Lokmer *et al.* 2008, Cannata *et al.* 2009, Cauchie *et al.* 2015). The results are described by the waveform correlation, where a high waveform correlation is indicative of a similar location and radiation pattern for two seismic events.

Cluster analysis was applied to characterize the LP waveforms belonging to the long-lasting increase phase (LP II, see Fig. 4). We aim to infer the time dependence of the most plausible LP sources at Lascar that can confer information about any precursory signal associated with the 2015 eruption. This requirement is fulfilled only by the OVDAS network, which was tested for the most stable time stations (LAS, QUE and PUN). The test was applied by subtracting the full signal contained in a 12 s window in which onset is defined 2 s earlier from the event time defined in the OVDAS seismic catalog. Therefore, whenever the waveform is not fully contained in the data or suffers from data gaps, it is not considered for further analysis. We tested the signals by applying different filters between 0.75 and 2.0 Hz and collected the waveforms in a folder for subsequent correlation. We iterated this procedure for the different spatial recording components of each station and computed the correlation matrix based on the waveform similarity cross-correlation value. Then, the correlation matrix, which hosts values in the range of [–1,1] for each event pair (ranging from –1 for anticorrelation to 1 for correlation, with 0 denoting no correlation), is transformed into a metric matrix by assigning a distance value of 0 to correlated waveforms and a value of 1 to uncorrelated waveforms. This matrix is used by a density-based clustering algorithm (Cesca *et al.* 2014) to identify a number of LP clusters showing similar waveforms with established parameters, thereby establishing clusters of at least 10 waveforms sharing a cross-correlation similarity value exceeding 0.75. Our aim in the application of this method is to search for the spatial component with the highest waveform similarity, independent of the number of resolved clusters. These similar waveforms are then used to interpret the seismic source and further investigate the temporal evolution of LP seismicity.

2.3 Seismic event location

The OVDAS catalog provides first rough VT hypocentral locations and no tentative LP locations. The VTs were located in real time by expert seismology analysts assuming two available velocity models. The model provided by Comte *et al.* (1994) was used for the period from January to December 2013; later, this model was updated with a new study provided by Dorbath *et al.* (2008) for the remaining period (January 2014 to December 2015). To unify the locations of VTs and LPs under one velocity model, we used a homogenous model assuming a v_P/v_S ratio of 1.73 with $v_P = 4.39\ \mathrm{km\,s^{-1}}$ and $v_S = 2.40\ \mathrm{km\,s^{-1}}$ (Bohm *et al.* 2002) for the first 5 km, which comprises the zone of interest in this study.

The VT relocation was performed for events that contained five phases and were recorded by at least four stations. *P* and *S* onsets were picked on raw data, and the hypocentral parameters were computed using Hypo71 (Lee & Lahr 1972). However, because the location of LPs is not trivial, we compare different approaches to locate these characteristic volcanic signals, as detailed below.

The characteristics of LP signals pose a challenge to the identification and accurate picking of first *P*-wave onsets as well as the recognition of *S* phases. The major practical consequence is that LPs cannot be located conventionally, and their hypocentral locations often suffer from large uncertainties (Lahr *et al.* 1994, Chouet 2003). A number of innovative methods have been proposed to locate LP sources based on the analysis of the waveform amplitude (Battaglia *et al.* 2003) and polarization (e.g. Cesca *et al.* 2008). Following these methods, we propose and test two new approaches in this study. The first technique is based on the coherent detection of anomalous amplitude and polarization attributes at multiple stations: this approach has been applied to a range of seismic signals (e.g. Grigoli *et al.* 2013, 2014), but it has never been applied

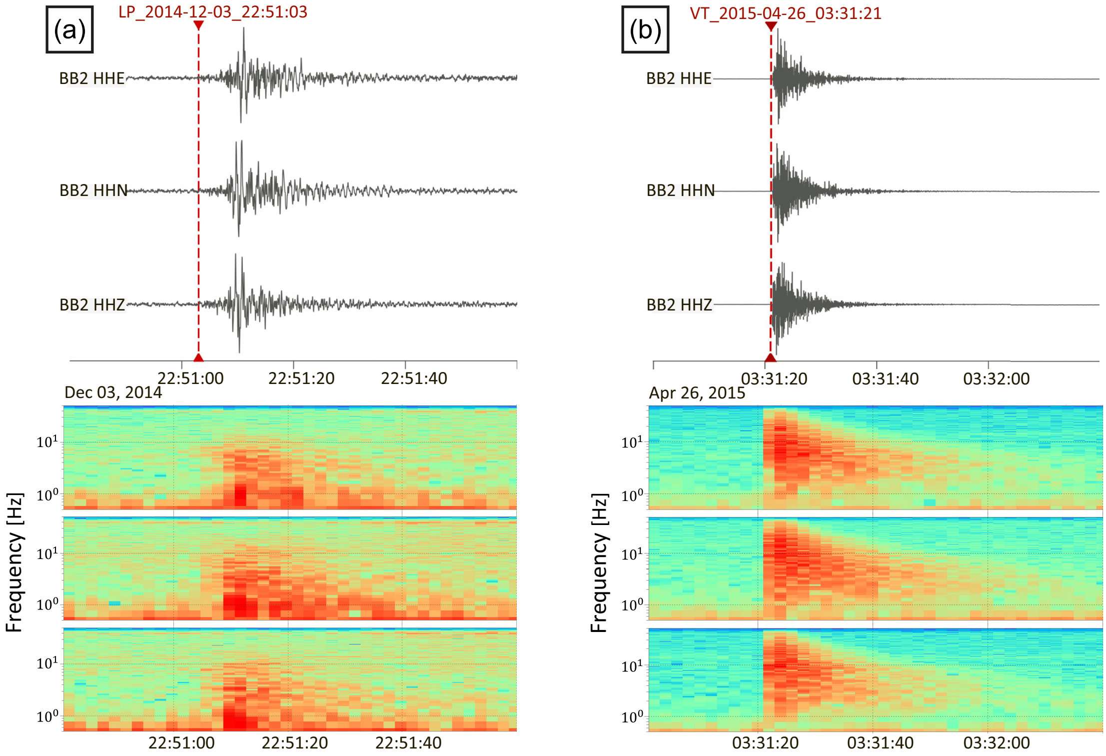

Figure 2. Seismic signals recorded at Lascar (top panel) and spectrograms (bottom panel). (a) Characteristic LP waveforms with frequencies in the band below 10 Hz. (b) Characteristic VT event with frequencies reaching 40 Hz.

to LPs heretofore. The second new approach relies on the cross-correlation of similar waveforms recorded at different stations and is tested with LPs for the first time in this study. The time period and hence the number of LPs chosen for the application of these methods were determined according to the availability of good-quality signals according the requirements of each method. The results and performance of these four methods are presented below.

2.3.1 Amplitude-based location of LPs

Source location methods based on the decay of seismic amplitudes with increasing distance to the source due to geometrical spreading and attenuation under the assumption of isotropic radiation patterns (Battaglia & Aki 2003; Battaglia *et al.* 2003) have been widely used to locate LP, VLP, explosion and volcanic tremor (Di Grazia *et al.* 2006; Kumagai *et al.* 2011; Taisne *et al.* 2011; Morioka *et al.* 2017). These methods are based on the simple observation that seismic amplitudes (using peak, median or mean absolute amplitudes) often exhibit a smooth spatial pattern after correcting for local amplification factors, which can be readily explained by the theoretical decay of surface or body wave amplitudes in a homogeneous medium; an inversion method can then be established to derive the location that best reproduces the observed peak amplitude pattern (Battaglia & Aki 2003).

We located the 196 most energetic LPs recorded by at least five stations between September 2014 and October 2015 based on the peak-to-peak amplitudes after applying a bandpass filter in the range of 1–10 Hz. As the location computed through this method uses the spatial distribution of seismic amplitudes, any amplification due to site effect must be removed. Thus, we estimated the site effect represented as the coda amplification factor to correct the seismic amplitudes, as proposed by Battaglia & Aki (2003). To this aim, we assume that the subsurface beneath the volcano is composed of several elastic layers locally characterized by different geometries and attenuation factors, which may locally affect waveform amplitudes and could affect the locations of LPs. To quantify the energy dissipation due to both intrinsic and scattering attenuation, we calculate the quality factor Q^{-1} (eq. 1) and minimize the location errors when compared with the theoretical amplitudes calculated for each station as a function of the station-hypocentre distance by iterating over values of the hypocentre. After the application of the coda amplitude regression, we chose 25 regional events with a satisfactory correlation coefficient ($R \geq 0.7$) that were registered by stations BB2, BB3, BB4, BB5, QUE and LAS, all of which are located more than 100 km from the volcano, and calculated the relative site amplification factors, using station BB2 (Fig. 1b) as a reference, which shows good-quality data.

$$Q = 2\pi \frac{E}{\delta E}. \tag{1}$$

2.3.2 Polarization-based location of LPs

While LP signals are emergent and first onsets cannot be easily identified, an increase in the signal amplitude is observed at most stations located on the volcano flanks, and this characteristic can be used to assess the polarization of the signal. Many authors have used the linear polarization of particle motions, even in the absence of an accurate velocity model, to locate the sources of seismic signals (including LP and VLP signals) at volcanoes (Del Pezzo *et al.* 1992; Neuberg *et al.* 1994; Neuberg & Luckett 1996; Battaglia *et al.* 2003; Marchetti & Ripepe 2005; Saccorotti *et al.* 2007; Cesca *et al.* 2008). The general approach is simple: either the three components of the seismogram or the two horizontal components only are considered to reconstruct the ground motion vector or its horizontal projection.

LP signals often show rectilinear particle motion observed either for the whole signal or for the first part of the signal alone, and this particle motion is assumed to correspond to a *P*-wave signal. At Lascar, the LP signals at some stations (e.g. BB3, BB4) show a linearly polarized signal for 1–2 s, although this polarization is lost in the later part of the signal, possibly due to the interaction between the seismic radiation and the volcanic topography. Assuming that the first part of the polarized signal corresponds to a P phase, which particle motion should point in the direction of the seismic source, the derived particle motion vector can be back-traced along its travel path, providing a range of potential locations. Performing this analysis for multiple seismic stations allows the hypocentral location (or the epicentral location if the analysis is performed on the horizontal components only) to be mapped: the source location can be found by minimizing the sum of the residuals among the observed and predicted polarization orientations. However, inverting the three-component ground motion vectors at a volcano requires surface corrections accounting for topography to be applied (Neuberg & Pointer 2000).

While the method described in Section 2.3.1 considers the data sets recorded by both networks (OVDAS and GFZ), here, we consider only a selection of 138 LPs recorded by the GFZ temporal network during the period from December 2014 to May 2015 (see Fig. 1). We assess the polarization of the signals for these events both for the horizontal components and for the thre-component recordings. We first use the two-component approach to discuss the epicentral locations of the LPs, and then extend the analysis to all three-component to further constrain their hypocentral depths. The processing is performed as follows. Particle motions are computed using 3 s long-time windows starting 1 s before the first visible amplitude increment after manual picking that corresponds to the first part of the detected LP signal. The seismic signals are then filtered, applying a 4th order Butterworth filter between 0.05 and 1.50 Hz. The polarization analysis is implemented on the three-component signal in the ObsPy library (Beyreuther *et al.* 2010) based on the work of Jurkevics (1988). In our implementation, we adopt the definition of rectilinearity given by Montalbetti & Kanasewich (1970) by first considering the two horizontal components to derive the backazimuth and then considering the radial and vertical components to derive the incidence angle. We consider only the signals whose rectilinearity coefficient is larger than 10. In such cases, the backazimuth and incidence angle are inferred, and the deformation vector is used to infer the potential range of locations.

2.3.3 *Coherency-based location of LPs*

Recent automated migration-based location techniques have been developed to detect coherent seismic signals at multiple seismic stations from continuous recordings (see Cesca & Grigoli 2015, for a review). Whereas these techniques are applied mostly to microseismic and regional seismicity data sets (e.g. Kao & Shan 2004, 2007; Gharti *et al.* 2010; Grigoli *et al.* 2013, 2014; Zeng *et al.* 2014), they may be suited for volcano seismology applications, particularly for locating LP events, given that they do not require any manual phase picking. One category of these coherency-based location algorithms is based on the concepts of the delay and sum of characteristic functions, which are positive time series derived from the observed waveforms depicting increments in amplitude, spectral or polarization attributes. The source location is performed using a coherence function, which is obtained by stacking the absolute amplitudes of characteristic functions recorded at different stations according to theoretical traveltimes over a 4-D spatiotemporal grid and then scanning a potential seismogenic volume for different origin times.

In this work, we sample the potential seismogenic volume extending spatially over dimensions of 15.3 km (east) x 10.8 km (north) x 10.0 km (depth) around Lascar volcano containing 2 212 001 gridpoints. The spatial sampling ranges between 85 m and 100 m depending on the axes. The volume extends from 6 km above sea level (a.s.l.) to 4 km below sea level. We use raw velocity traces sampled at 100 Hz. We applied this method to 256 LP events recorded between September 2014 and April 2015; beyond this period, the network was operated discontinuously and no longer fulfilled the conditions for operating stations. For the application of this method we adopted the two characteristic functions proposed by Grigoli *et al.* (2014): first onsets (i.e. *P*-phases) are detected through the short-term average/long-term average (STA/LTA, with a short time window of 0.25 s and a long-time window of 0.75 s) of the vertical energy characteristic function, sensitive to the *P*-phase amplitude increase on the vertical component; furthermore, we aim to detect *S* phases through the STA/LTA (with the same parametrization) of a second characteristic function, which is sensitive to the *S*-wave polarization, based on the principal component analysis technique. Theoretical traveltimes are computed for *P* and *S* waves, assuming the homogeneous velocity model described in Section 2.3 (called M1) and for a second model denoted M2 ($v_P = 5.51$ km s^{-1}, $v_S = 3.19$ km s^{-1}), in which the standard v_P/v_S ratio is also 1.73 (Bohm *et al.* 2002). This approach circumvents the challenging identification of P and S phases of LPs, by relying instead on the detection of anomalous amplitude and polarization patterns at multiple stations.

2.3.4 *Cross-correlation-based location of LPs*

The cross-correlations of filtered waveforms recorded at the same stations for different events can be used to resolve the relative locations of seismic sources producing similar waveforms at each station. The development and application of double-difference techniques (Waldhauser & Ellsworth 2000; Waldhauser 2001) based on the cross-correlation approach has produced substantial advances in improving earthquake locations by suppressing most location uncertainties due to unknown velocity structures without the use of station corrections (Schaff & Waldhauser 2005). The cross-correlation technique has been applied to a variety of seismological observations to derive relative hypocentral locations, including seismic signals at volcanoes (Matoza *et al.* 2013) and specifically LP events (Matoza *et al.* 2014). In the original approach by Matoza *et al.* (2013), cross-correlation was performed among the *S* phases of event pairs to infer the differential *S* time to locate different seismic signals at volcanoes.

In this work, we use cross-correlation in a different way. Instead of correlating pairs of events at a common station to infer their relative locations, we correlate the waveforms recorded at different stations for the same event to infer the traveltime differences and, based upon those differences, the absolute event locations. This approach is possible here only because the observed vertical components of LP signals appear highly similar at most stations deployed on the flanks of the volcanic edifice (Fig. 3). The high waveform similarity on the vertical components has further implications in terms of the source radiation pattern, which will be discussed later. Under this condition, we can compute differential *P* arrival times at each station

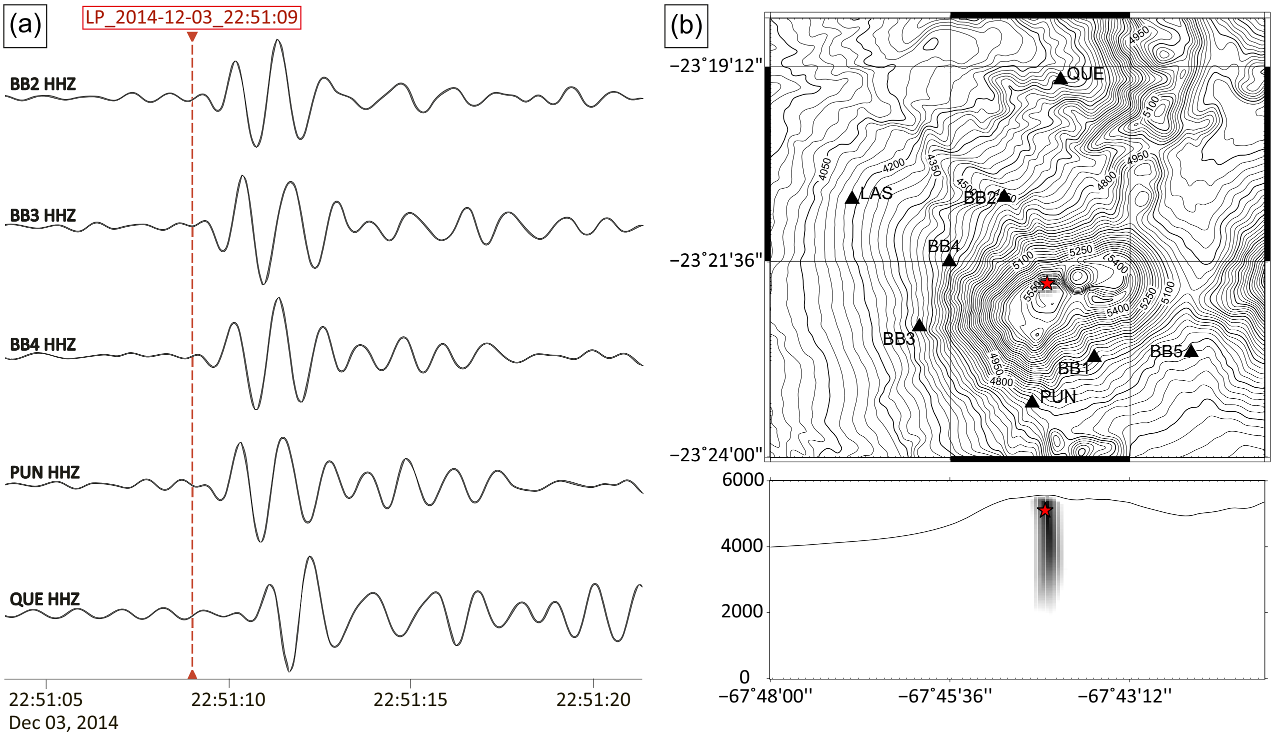

Figure 3. (a) Vertical component of one characteristic LP event after applying a passband filter at band frequencies of 0.1–1 Hz, revealing a high waveform similarity among different stations. This feature is implemented using cross-correlation to derive the interstation differential arrival time. The event onset waveform, including the day and time are indicated in red. Interstation cross-correlation is performed on a 10 s long time window (filtered vertical component) starting at the picked onset. (b) Map and profile views of the synthetic test showing the uncertainties of the cross-correlation method. The red star indicates the location obtained using our velocity model (see Section 2.3) and the greyscale its corresponding temporal residual depict a high accuracy of the epicentral location and a high uncertainty in the hypocentral constraint.

pair for each considered LPs and constrain the absolute source location with the differential traveltime and location of each station. For this analysis, we considered raw velocity waveforms for the vertical components filtered using a 4-pole Butterworth bandpass filter in the frequency band of 0.1–1.0 Hz and considering a window length of 10 s starting before the first amplitude peak increase for a 1-D velocity model. We next performed a grid search for any potential location using the same grid as that used in the coherence-based location approach while assuming a range of homogeneous *P*-wave velocities between 2.5 and 4.5 km s^{-1} and minimizing the differences among the estimated and theoretical differential *P* arrival times. Out of all the detected LPs, we considered only those with sufficiently high cross-correlations (above 0.8) estimated for at least 8 station pairs, thereby reducing the data set to 83 LPs in the time span from December 2014 to May 2015, which constitutes the period with continuous data recording and the highest network density (see Fig. 1). We performed a synthetic test to assess the spatial resolution of this location approach: we assumed a shallow LP source beneath the crater region and computed differential arrival times at the used station pairs while assuming a velocity model with a *P*-wave velocity of 4 km s^{-1}. Then, we applied our location approach, estimated the theoretical differential times (instead of deriving them through waveform cross-correlation) and mapped the spatial distribution of residuals (shown in greyscale in Fig. 3b). Our results indicate a good epicentral resolution but a relatively low depth resolution. We also executed a second test by deriving the LP event locations using velocity models perturbed in the range between 2.5 and 4.5 km s^{-1}: the result was similar in the sense that we could correctly retrieve the epicentral location while assuming a perturbed velocity model, but shifts were introduced into the resulting depths. This is a novel method, and the results are comparable to other techniques.

3 RESULTS

3.1 Temporal evolution of LPs and VTs

Based on the significant variations in the numbers of LPs and VTs throughout the entire period covered by this study, we subdivide their temporal evolution into 7 seismicity phases of activity at Lascar volcano (LP I, low I, VT I, low II, VT II, LP II and low III). Fig. 4 graphically outlines these phases by means of the daily rates of LP events and the cumulative number of both LPs and VTs. The low, steady VT activity rate ($<$1 event/day) is obviously exceeded during two, short-duration bursts of activity. The first and largest burst occurred in June–July 2013 (phase VT I in Fig. 4, ∼300 events), accompanied by a weak increase in LP activity. The second and weaker phase of VT activity struck in September-October 2014 (phase VT II, 9 events). Phase VT II was accompanied by crater incandescence and effectively coincided with the subtle beginning of a sustained long-term anomaly of LP events; the remarkably long-term LP II anomaly began in September 2014 and lasted for approximately 14 months, culminating in the eruption on October 30, 2015. The LP seismicity rate appears to be strongly modulated in time: during the initial phase corresponding to VT II, LP activity was rather weak, but the activity slowly and steadily increased thereafter until reaching a peak of 13 events/day in May–June 2015 and then slowly decreased to $<$5 events/day while approaching the 2015

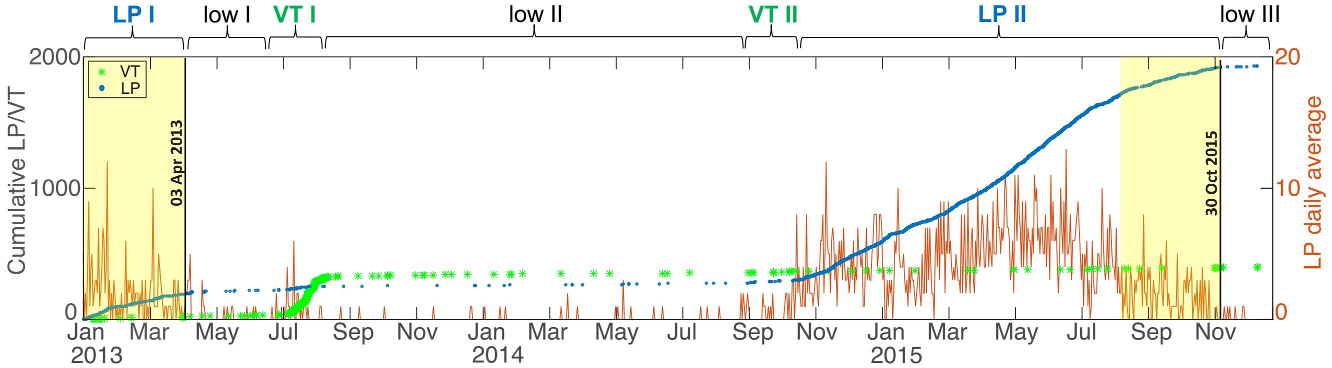

Figure 4. Temporal evolution of LP (blue dots) and VT (green stars) events recorded in the period covered by this study. The daily average of LP events (shown in orange) reveals 10 months of an unusually high average preceding the 2015 eruption (LP II) associated with an increasing period of LP activity. The subsequent phase shows a decrease in the rate of LP events starting 2 months before the eruption; this pattern is also observed for the 2013 eruption (LP I), where the activity declines rapidly after the event. Similar patterns in the decreasing LP activity period preceding the 2013 and 2015 eruptions are shaded in yellow.

eruption. After this eruption, LP activity dropped substantially to the previous phase of quiescence (phase low III). Interestingly, similar decay in the anomaly of LP events is observed just before the 2013 eruption (phase LP I); unfortunately, the catalog is incomplete at preceding dates and therefore does not allow a full comparison of precursor LP activities prior to the 2013 and 2015 eruptions.

Sections 3.2 and 3.3 describe the results for the most interesting VT and LP phases, discussing waveform similarity (LP II) and hypocentral locations (VT I, VT II and LP II). The LP II phase is especially attractive due to the abundant number of events, recorded in a phase of densified seismic network (see Fig. 1) and in view of its role in the preparatory phase of the 2015 eruption.

3.2 LP waveform similarity

The iterative application of a cluster analysis, separately performed for all spatial components of stations QUE, LAS and PUN provides evidence for one single cluster of similar events. This is better resolved using seismic data of stations PUN and QUE, with the last one showing the most clear result and highest waveform similarity. This cluster remains undetectable using the data from station LAS, probably due to the lower signal-to-noise ratio at this site. The final clustering results concern only events recorded at more stations and are clustered on different components simultaneously. This reduces the starting data set to 450 LP events and reduces the number of clustered events to 72. While losing many events, we can argue with relatively safety that these clustered events represent a similar process since a strict control has been implemented insomuch that these LPs have similar waveforms recorded at different stations and on different components. This high waveform similarity indicates a similar location and radiation pattern but also depends on the quality of the signal: we found that clustered events typically show larger amplitudes than unclustered events. This suggests that unclustered events may also be generated by a similar mechanism, but this mechanism is associated with weaker and noisier signals, and the noise affects the waveform similarity.

The results are illustrated in Fig. 5 for station QUE. Clustered LP waveforms with high similarity are shown individually according to their occurrence in time, and they are stacked as well; by stacking similar waveforms, we enhance the common LP signal against random noise and thus improve the signal-to-noise ratio. Stacked waveforms are characterized by clearly visible amplitude modulations (e.g. on the north component of station QUE), which could be controlled by the presence of different seismic phases, the interaction between the seismic radiation with the topography or other strong impedance contrasts, or by the complexity of the source time function. Depending on the waveform amplitudes and seismic noise contamination, the number of clustered signals changes from case to case.

We observe no temporal variation of the waveform similarity, which could suggest a spatiotemporal migration or a temporal change of the source mechanism. The individual plots of the waveforms support the occurrence of an LP event produced by the same source throughout the entire phase LP II (clustered events occur from September 2, 2014, to October 26, 2015). This discards the possibility of employing the temporal evolution of the source as an indicator for a preparatory eruption phase and instead alludes to the recurring occurrence of the same process with a similar source location and source mechanism that is responsible for the observed similar LP signals. This process is likely to be active over several months, although with a variable activity rate.

3.3 Seismic event locations

Fig. 6 shows the results obtained by applying the first three location methods described previously. From the amplitude based method (Fig. 6a), we observe the LP sources to be located within a compact and shallow cluster confined at depths from 2 to 5 km below the summit, which has an altitude of 5592 m. However, the cluster location shows a significant offset of approximately 1 km to the northeast with respect to the summit of Lascar, where no surface expression of degassing or surface fracturing has been observed. It is worth noting that, due to the limited data availability and waveform quality, most events have been located using a station geometry with poor azimuthal coverage.

Upon applying the polarization-based method, only a limited number of stations show clear linear polarization; furthermore, the mentioned rectilinearity condition is rarely met at multiple stations simultaneously for the same event. In particular, stations located on the western flank of the edifice show higher signal polarization, while the polarization is lost to the north and south of the crater and at larger distances. According to abovementioned, the filtered LP signals often appear to be linearly polarized at station BB4 and,

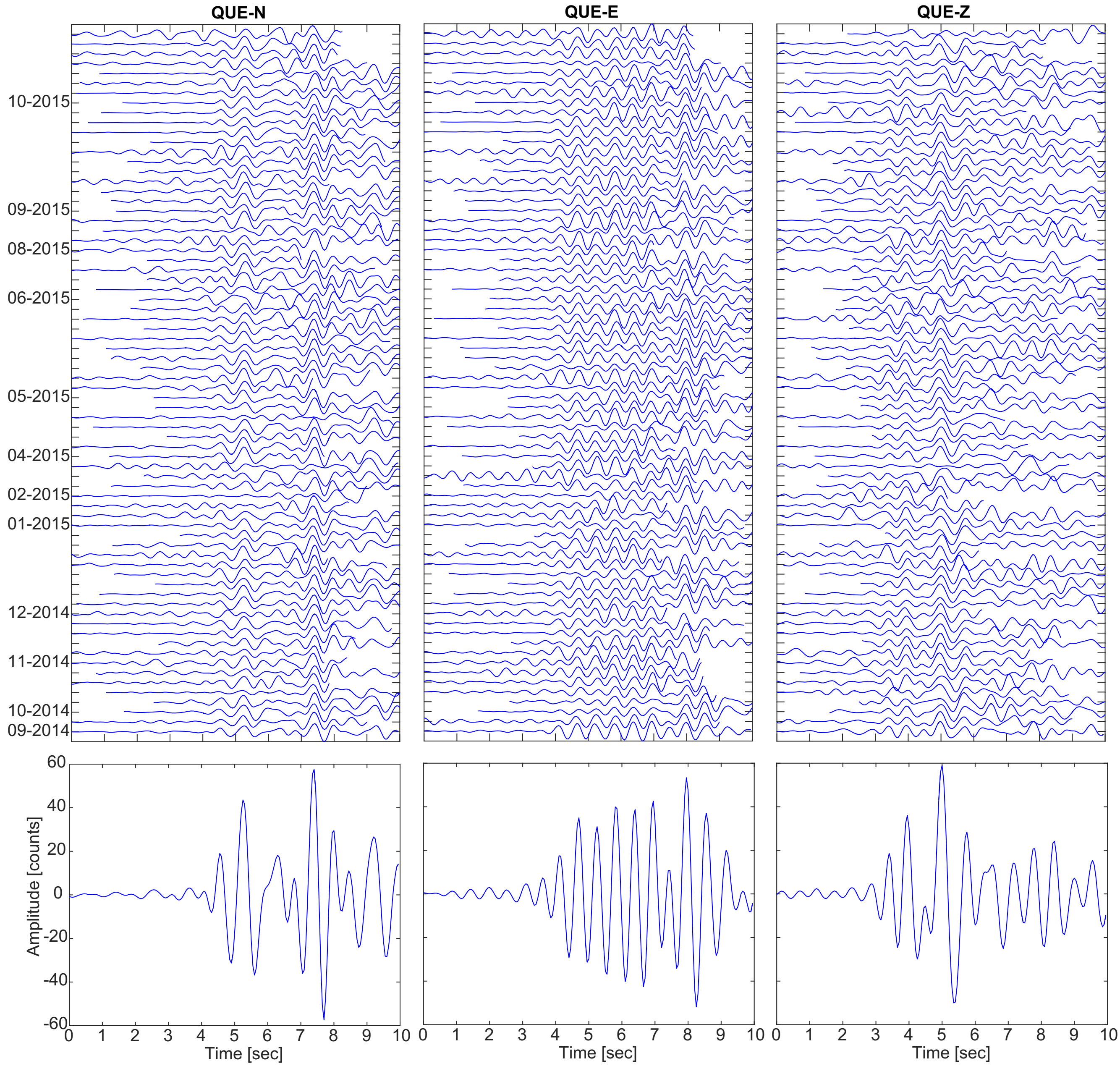

Figure 5. Similar LP waveforms on the north, east and vertical components recorded at station QUE. The waveforms correspond to 72 events derived from cluster analysis of the QUE-E component aligned upon cross-correlation, and the respective waveform stacks are shown in the bottom row for the three components. The occurrence dates are sorted on the vertical axis by month.

in some cases, at stations BB3 and BB2 (see examples in Fig. 6b). High signal polarization is rarely observed at other stations, possibly because of their larger epicentral distances and/or topographic effects. At station BB4, 75 computed backazimuths vary between 85 and 120°, while at station BB3, 14 backazimuths range between 48° and 94°. Station BB2 shows highly variable and incompatible particle motion directions and thus does not add a further constraint on the source location. These results are compatible with epicentral locations within an elongated EW-trending region just west of the crater rim in the vicinity of the summit or further eastward. Moreover, the incidence angles restrict the depth beneath the volcano dome in the range of altitudes between ~2.5 km and the summit. An interesting observation concerns the variability of polarization at different stations, which is sometimes higher at either BB4 or BB3 but rarely simultaneously. One possible explanation would be variability in the hypocentral location coincident with different wavefield interactions with the volcanic topography or other structural heterogeneities, thereby disrupting the observed polarization at one station or the other depending on the source location. An alternative explanation may concern the variability of the focal mechanisms and radiation pattern and thus a different geometry of the seismic sources with higher polarization of the *P* signal at different azimuths. In these conditions, rather than deriving absolute locations for single events, we could find only the approximate

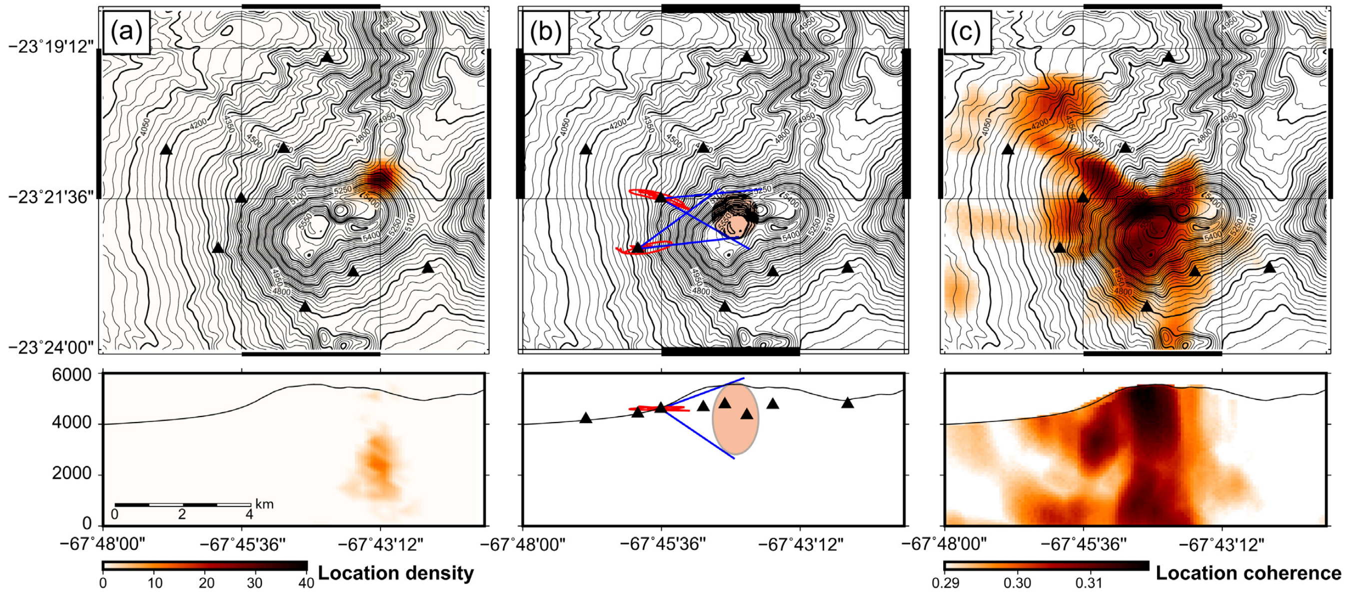

Figure 6. Location results using three different methods to compute the hypocentral locations of the LPs in map view (top) and E–W cross sections (bottom), where the black triangles denote broad-band stations. (a) Amplitude-based LP locations, where the colour bar denotes the density of hypocentral locations. (b) Polarization-based LP location based on the rectilinear polarization of particle motions at stations BB3 and BB4 (the particle motions are plotted in red for two LPs) pointing to a source region (light brown ellipse only for illustration) located NE of BB3 and ESE of BB4 (blue wedges). (c) Coherence-based LP locations, where the color bar denotes the cumulative coherence of all studied LPs.

location of the LP seismogenic source under the assumption that these LP events are generated within a relatively confined volume.

The application of the coherence-based method provides a whole set of hypocentral locations. The locations were calculated using the general model M1 (see Section 2.3) and a secondary model M2 (see Section 2.3.3); M1 showed a better performance in general, providing higher coherence values for most events. Although these events are more scattered than the locations obtained from the amplitude-based method, we find that an important majority of the coherence-based locations reside within a small area of high coherency. As a result, stacking the coherence matrices for all processed events (following Cesca *et al.* 2016) reveals a region of high coherence at a very shallow depth extending from the summit down to ∼3 km (Fig. 6c) exactly below the summit of Lascar volcano (∼2.5 to 5.5 km a.s.l.), and these findings are in very good agreement with the independent results of the polarization-based location.

Finally, the cross-correlation method revealed the majority of locations for a velocity of 4.0 km s^{-1}, consistent with the velocity model proposed for the applications of this approach ($V_P = 3.9$ km s^{-1}, see Section 2.3). Thus, we fixed this velocity model and repeated the inversion for the hypocentral location only. The resulting LP event locations are shown in Fig. 7 together with 52 relocated VTs that correspond to increased activity during phases VT I and VT II (see Fig. 4). The correlation-based LP locations are in general agreement with those relying on the polarization and coherence (Figs 6b and c). However, they identify a much more compact cluster of locations with epicentres that are aligned along an ENE–WSW direction. In depth, the cluster extends from the western rim of the active crater (crater A in Fig. 1d) down to an altitude of at least 3.5 km along a narrow stripe, delineating a path along which fluid and gas ascend in the uppermost part of the plumbing system. Most locations, including all of those with lower residuals (below 0.1 s), are found in the shallowest 2 km.

The VT locations are more scattered than the LP locations; most of them occur in correspondence with the LP cluster but at larger depths (between ∼0 km and ∼3 km a.s.l.). The VT events have a maximum magnitude of 2.3, and the hypocentral errors in the horizontal (Erh) and vertical (Erz) components are smaller than 1.6 and 4.0 km, respectively, with rms values below 0.6 s. Finally, from the entire image of LP and VT event locations, we can observe a transition phase from VT to LP sources, which would indicate that the uppermost region of brittle processes is found at an altitude of approximately 1.5–3 km and thus at least 3 km below the summit.

4 DISCUSSION

This is the first detailed seismic study focused on Lascar volcano in many decades, and the results reveal the presence of approximately 2000 LP and 350 VT events. To confirm standard VT event location methods, we applied the LP event location methods presented in the literature and proposed a new strategy for obtaining reliable results in a difficult volcanic environment.

The results are in general agreement and suggest the presence of a shallow hydrothermal system with a deeper elongated arrangement that can be interpreted as a plumbing system, which would coincide with the findings of independent studies, as further discussed below. However, before debating the implications of the deeper structure under Lascar volcano, we discuss the performance of the LP location methods.

4.1 LP location methods

With this well-covered data set, we were able to describe the intereruption phase of Lascar volcano, giving a complete analysis of the most typical seismic waveforms in terms of their source locations and mechanisms. For this purpose, we applied four different methods to locate the most abundant events (LP) recorded. Three of the applied location methods (i.e. the polarization-, coherence- and

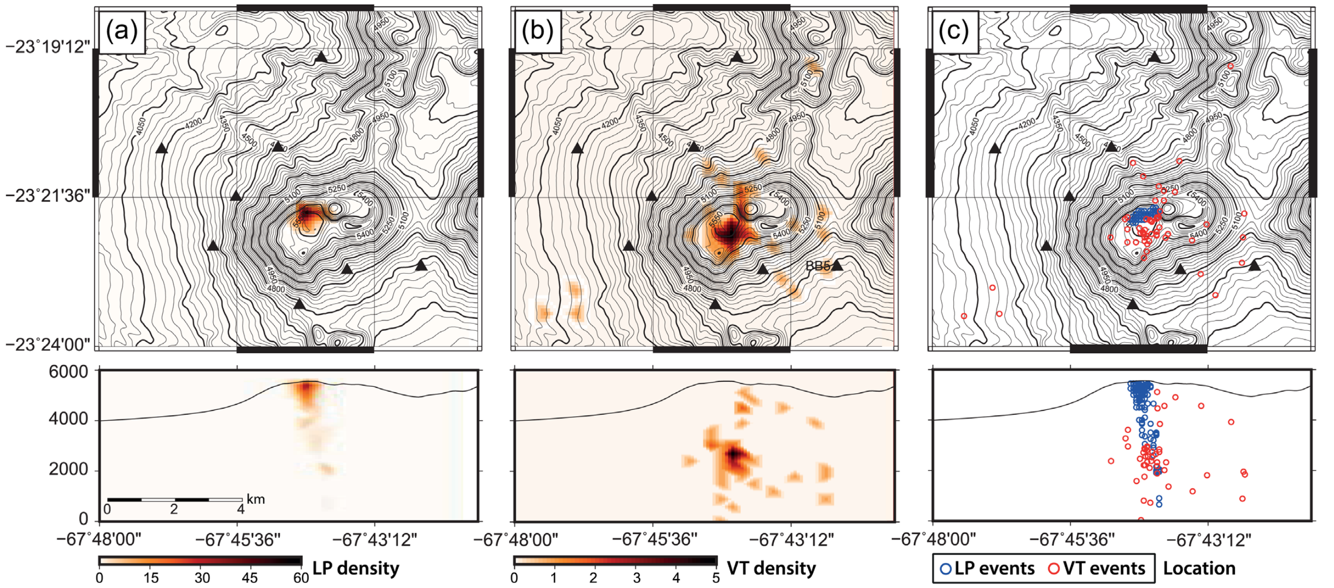

Figure 7. Cross-correlation-based LP locations and standard VT locations shown in map view (top) and E–W vertical cross sections (bottom). (a) LP location density. (b) VT location density. (c) Hypocentral locations of LPs (blue) and VTs (red).

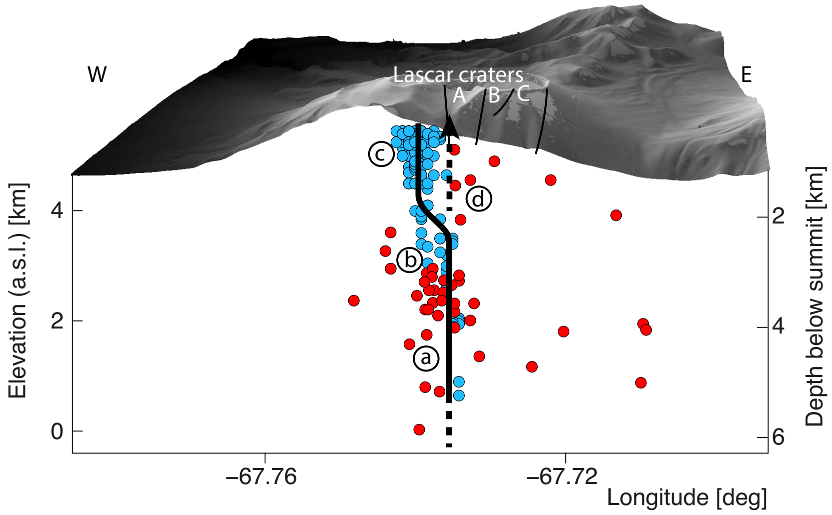

Figure 8. Schematic representation of the Lascar topographic profile and path geometry imaged by the LP (blue dots) and VT (red dots) hypocentres. The black thick line represents the three main zones recognized from the hypocentral distribution: (a) subvertical deep conduit and VT cluster beneath zone (b), (b) bending zone where the LP trend changes and (c) shallow LP cluster. The dashed arrow (d) represents the expected path towards the active crater A. Black solid thin line are the fractures associated with the nested summit crater rims (A, B and C) from de Zeeuw-van Dalfsen *et al.* (2017) and Richter *et al.* (2018).

cross-correlation-based methods) agree on the stationary hypocentral locations of the LP events at shallow depths beneath the volcano summit (Figs 6b, c and 7a). However, the hypocentral locations achieved using the (commonly used) amplitude-based method are slightly shifted laterally towards the northeastern flank of Lascar volcano (Fig. 6a). The hypocentral accuracy depends, among other factors, on the network geometry, velocity structure and quality of arrival time data. Hence, this lateral shift could result from the limited number of stations and poor azimuthal coverage: the two stations closest to the summit were not considered in this analysis due to the presence of a high seismic noise level (probably produced by the very strong winds in this region). This effect was already discussed elsewhere, for instance, at Etna volcano, where the exclusion of two stations near the summit resulted in the spreading of epicentres in comparison with the results based on the full network (Zobin 2012). Additionally, using regional events rather than local events to estimate the amplitude corrections may bias the results of the amplitude-based location. However, we discard the effect of the velocity structure because the amplitude-based method does not require a velocity model or *P* phase picking. On the other hand, the coherence and polarization based methods defines a seismogenic region where it is relatively plausible to find LP sources (at shallow depth from the volcano summit down to ∼3 km a.s.l.), but they do not provide precise locations. In contrast, the cross-correlation of waveforms recorded at different stations, provides more accurate and solid results, that match qualitatively the hypocentral region identified by the polarization and coherence-based methods. Thus, this method was successfully applied at Lascar despite the fact that this approach is rarely used at volcanoes and is possible only with a certain source mechanism geometry. The correlation-based method resulted in robust locations for the chosen velocity model with a high accuracy in the epicentral solution, while the depth resolution was less accurate (Fig. 3b). Remarkably, these results do not significantly change by perturbing *P*- and *S*-wave velocities, and provide similar LP locations for a range of tested velocity models. In this work, we suggest a comparative analysis of these different location methods as a robust approach to overcome the challenges associated with locating the hypocentres of LP events.

4.2 Precursory signals

This work highlighted an almost complete LP quiescence (Fig. 4) lasting about 16 months after the 2013 eruption (May 2013 to August 2014). This was followed by a subtle, but long-lasting increase in LP activity (September 2014 to July 2015) before the number of LPs gradually decreased again (August 2015 to October 2015). Another eruption occurred on 30 October 2015. After the eruption we observed again the start of a new LP quiescence period, with almost complete absence of LP activity. The 2015 LP decrease pattern preceding the most recent eruption was also observed before the 2013 eruption with a comparable occurrence rate of LPs while approaching the eruption time. The seismicity therefore indicates that the volcano was in an elevated stage of activity, but it did not display a sharp culmination of events shortly before erupting. This peculiar modulation appears as a preparatory phase of the system prior to an eruption as short-term swarms of precursory activity described, for example at Chichón volcano, Mexico; Mt Pinatubo, Philippines and Redoubt, Alaska (Chouet 1996). Likewise, Mt Etna volcano, in Italy has exhibited a similar LP rate pattern prior to the May 2008 lava fountain episode (an LP period decrease over two weeks, Bonaccorso *et al.* 2011) as well as prior to the November 2007 strombolian activity and subsequent lava fountain episodes (LP increase/decrease and variation of other signals over a period of two months, Patanè *et al.* 2008). The LP activity therein was explained as a result of the transport/discharge of gas-rich magma. The main differences between the LP modulations at Lascar and those at Mt. Etna concern the shorter duration of the latter (weeks at Etna versus months at Lascar) and their culmination into lava eruptions compared with the weak explosions accompanied by ash emissions at Lascar volcano.

Redoubt volcano has also shown similar LP precursors over both short (hours to days, Chouet *et al.* 1994) and long (months to years) time periods. For example, a 6–7 months LP anomaly preceded the 23 March 2009, Redoubt eruption. Then, two months before the eruption, the LP activity dwindled and began to display tremor-like activity. This process has been explained as a protracted period of slow magma ascent, followed by a rapid increasing pressure over a short period (Roman & Gardine 2013). However, we do not observe exactly the same evolution at Lascar (i.e. the change from LP to tremor-like activity); in the last few months, the LP activity at Lascar decreased. Possibly at Lascar, the rising fluids experienced the following scenarios: (i) they were blocked by a closed fluid path, possibly associated with crater subsidence (González *et al.* 2015; Richter *et al.* 2018); (ii) ascending fluids propagated into a very weak material (although we would expect tremor-like signal in this case) or (iii) the ascending fluids and/or magma stalled. In the third case, an important question must be raised: why did the eruption occur? It is possible that such an eruption occurred not to further increase the pressure from below but rather as the result of an external trigger, such as rainfall leading water–magma interaction. The details of this eruption must be elaborated in future works, offering the chance to establish patterns in volcano monitoring data and assess the volcanic hazard over both short and long time scales.

4.3 Implications of the similarity among seismic waveforms

While we could not perform an accurate investigation of the source mechanism in this work, the observation of similar vertical component waveforms at different azimuths suggests a radially symmetric radiation pattern comparable to the oscillation of, for example a vertical conduit, a spherical volume or a horizontal crack. Given the spatial distribution of the hypocentres along a subvertical path, the hypothesis of the oscillation of a vertical conduit appears to be the most plausible. The relatively compact region of shallow LPs depicted by their hypocentral locations, the high waveform similarity and the lack of their spatiotemporal migration throughout the entire LP II phase support the common origin of the LP signals (Fig. 5). Our results suggest the repetition of a mechanism stationary in time, which is compatible with the oscillation of a vertical conduit or fracture due to gas flux, thereby reflecting pressure fluctuations, as proposed by Chouet (1996). High LP waveform similarity over a long time span was also observed during a long-term period of unrest following the April–May 1999 eruption of Shishaldin volcano, Alaska (Petersen *et al.* 2006), where the LP events revealed a high level of similarity over several months. Similarly, sustained LP activity at Mt Etna maintained significant similarity among spectra and waveforms, which agrees with our interpretation of the resonance of a fluid-filled cavity as a vertical conduit (Saccorotti *et al.* 2007).

4.4 Implications for a plumbing system and geothermal fluid path

Our locations show that most LP hypocentres are clustered in the first 2 km below the crater within the dormant edifice next to the active crater. This finding coincides well with the location of a high-conductivity layer 1 km beneath the summit interpreted as fluids within a hydrothermal system resolved by a previous magnetotelluric study (Díaz *et al.* 2012).

VTs have been located even deeper beneath the volcanic edifice belonging to the VT I and II swarms. The VT I swarm displays stand-alone VT swarm activity neither preceded nor followed by any other seismic or geophysical anomaly. In contrast, VT II precedes the beginning of the long-term LP anomaly. Based on their hypocentral locations, these VTs could be associated with brittle processes accompanying fluid ascent at some depth. Comparatively, a swarm of VTs preceded the LP activity at Campi Flegrei, Italy, associated with a hydrothermal origin (Cusano *et al.* 2008). Similar to our study, the VTs were rather outspread and occurred at a greater depth, which was interpreted to cause an increase in rock permeability, thus favoring the fluid mobility that caused the LP activity that was followed by an increase in thermal emissions and gas fluxes. Nevertheless, we know very little about the chemical variability of the hydrothermal system at Lascar, as this is beyond the aim of this study. We conjecture that the spatiotemporal distributions of VT and LP events seem to reflect a process that initiated with deep VT sources associated with the failure of the rock due to the concentration of stress, indicating the first sign of volcano activity, followed by the LP events located at relatively shallow depths, reflecting the instability of the volcanic system and providing early warning of a likely eruption.

Cusano *et al.* (2008) also found the spatial spreading of LP locations by imaging a subvertical path consistent with a fluid-filled crack observed from moment tensor inversion, and their findings are compatible with our results. Despite the depth resolution being lower than the epicentral accuracy of our method, we assume that the LP obtained by waveform cross-correlation delineate a conduit-like geometry down to ∼5 km below the summit adjacent to active crater A (Fig. 8). This fluid path can be divided into three main zones. The lowest 3 km shows a subvertical conduit located beneath the dormant western edifice (Fig. 8a), whereas the central stretch is characterized by hypocentres arranged in a dipping cluster (Fig. 8b), and most of the event locations are grouped in the shallowest 1 km in an elongated SW–NE cluster (Fig. 8c). The VT cluster just beneath the central stretch of LPs supports our previous suggestion about the spatiotemporal distribution of both types of events. We hypothesize that this deviatory path could be associated with the rock permeability attributed to the effect of the VT cluster, similar to Cusano *et al.* (2008), and possibly attributed to potential stress reorientation causing the migration of shallow seismic activity towards the dormant western edifice (from (d) to (c) in Fig. 8]. We propose three plausible mechanisms: (1) anisotropy in the bending zone could contribute to the creation of an inclined fluid path, as was confirmed experimentally by Gressier *et al.* (2010); (2) an unloading effect produced by the deep active crater A could produce the geometrical deviation of the fluid path, as was explained numerically by Maccaferri *et al.* (2011) and was analogically modelled for dykes propagating beneath calderas by Gaete *et al.* (2019) and (3) morphological changes due to constant subsidence and nearly E–W movement of the old nested crater towards the active one (Richter *et al.* 2018). Now, the remaining question is whether the path imaged through the LPs can also provide us clues about the migration of eruption activity towards the dormant edifice, which would suggest shallow LP locations.

Finally, the seismic data reveal no evidence for a major magma chamber, supporting the shallow hydrothermal system region proposed by Díaz *et al.* (2012). This could also explain the absence of major edifice-wide deformation in the geodetic data (Pritchard & Simons 2002), as the observed surface deformation is associated mainly with geomorphological changes (de Zeeuw-van Dalfsen *et al.* 2017; Richter *et al.* 2018). In conclusion, the eruption cycle at Lascar volcano appears to be currently driven by the pressurization of a hydrothermal system rather than by a magmatic system.

5 CONCLUSION

In this work, we use the permanent and temporary seismic deployments at Lascar volcano, Chile, to locate and discuss the spatiotemporal evolution of seismicity at this volcano over a time period of approximately 3 yr, which includes two eruption events. Following a detailed analysis, the seismicity is characterized mostly by LPs and VTs originating at a relatively shallow depth beneath the volcanic edifice. We compare a range of different location techniques based on amplitude, polarization, coherence and cross-correlation waveform features to better assess the hypocentral locations of the LPs. Three of the four location methods provide results that agree on a shallow region where it is more plausible to find the LPs, while the waveform cross-correlation method depicts absolute and robust events locations with a high epicentral accuracy but a relatively low depth resolution. The analysis is combined with waveform similarity and clustering evaluations to investigate the spatiotemporal evolution of LP sources and the presence of more waveform clusters, resulting in the resolution of a single type of signal and thus a single process responsible for the LP activity.

The data suggest an alternation between LP quiescence and activity period, this second one potentially preceding the Lascar eruptions. We observed in particular a preparatory period of ∼14 months preceding the 2015 eruption (VT II and LP II) starting with the first VT swarm in August 2014 and continuing with a sustained LP activity. The VT sources are located below the volcanic edifice at a depth of 3 km below the summit. We hypothesize that the VT signals are the result of brittle processes accompanying fracturing in response to gas and magmatic fluid transfer from depth to the uppermost plumbing system. The VT activity lasted for approximately 2 months and was accompanied by a subtle increase in LP activity. This LP activity, which continued until the eruption, gradually increased with time, reaching the highest event rate from October 2014 to July 2015. The LPs from the LP II phase are located below the summit and just above the VT seismogenic zone, extending along a narrow subvertical region down to a depth of ∼5 km that we suggest is the geometry of the volcanic conduit, excluding the presence of a magma chamber. Similar LP waveforms denote the repeated activation of a similar source process throughout the entire LP II phase, compatible with the resonance of a vertical conduit. In the last phase (August to October 2015), the LP activity declined again in preparation for the 2015 eruption. The LP seismicity rate during the last few months before the 2015 eruption was similar to that before the 2013 eruption, which could have implications for a volcanic hazard assessment. According to the evolution of LPs at the time of the 2015 eruption, the volcanic system appeared to have reached similar conditions to those at the time of the 2013 eruption. However, a strong increase in precipitation before the 2015 eruption may have acted as final trigger and may have controlled the eruption dynamics in its final phase.

ACKNOWLEDGEMENTS

This is a contribution to VOLCAPSE, a research project funded by the European Research Council under the European Union's H2020 Program/ERC consolidator grant n. [ERC-CoG 646858]. This research was supported by the German Research Centre for Geosciences, GFZ and by the program Forschungsstipendium für Doktorat from Deutscher Akademischer Austausch Dienst DAAD awarded to AG. We thank the field crew making this study possible, namely Martin Zimmer, Christian Kujawa, Stefan Mikulla, Jacqueline Salzer, Mehdi Nikkhoo and Nicole Richter.

REFERENCES

Asch, G., Kurt, W., Hellweg, M., Seidl, D. & Rademacher, H., 1996. Observations of rapid-fire event tremor at Lascar volcano, Chile, *Ann. Geophys.*, **39,** 273–282.

Battaglia, J. & Aki, K., 2003. Location of seismic events and eruptive fissures on the Piton de la Fournaise volcano using seismic amplitudes, *J. geophys. Res.*, **108,** 2364.

Battaglia, J., Got, J. & Okubo, P., 2003. Location of long-period events below Kilauea Volcano using seismic amplitudes and accurate relative relocation, *J. geophys. Res.,* **108,** 2553.

Bean, C.J., Barros, L. De, Lokmer, I., Métaxian, J.-P., O' Brien, G. & Murphy, S., 2014. Long-period seismicity in the shallow volcanic edifice formed from slow-rupture earthquakes. *Nat. Geosci.,* **7,** 71–75.

Beyreuther, M., Barsch, R., Krischer, L., Megies, T., Behr, Y. & Wassermann, J., 2010. ObsPy: a python toolbox for seismology. *Seismol. Res. Lett.,* **81,** 530–533.

Bohm, M., Lüth, S., Echtler, H., Asch, G., Bataille, K., Bruhn, C., Rietbrock, A. & Wigger, P., 2002. The Southern Andes between 36° and 40° S latitude: seismicity and average seismic velocities. *Tectonophysics,* **356,** 275–289.

Bonaccorso, A., Cannata, A., Corsaro, R.A., Grazia, G. Di, Gambino, S., Greco, F., Miraglia, L. & Pistorio, A., 2011. Multidisciplinary investigation on a lava fountain preceding a flank eruption: the 10 May 2008 Etna case. *Geochem., Geophys. Geosyst.,* **12,** 1–21.

Bredemeyer, S., Ulmer, F.G., Hansteen, T.H. & Walter, T.R., 2018. Radar path delay effects in volcanic gas plumes: the case of Láscar Volcano, Northern Chile. *Remote Sens*., **10,** 1514.

Burchardt, S. & Galland, O., 2016. Studying volcanic plumbing systems – multidisciplinary approaches to a multifaceted problem, in *Updates in Volcanology - From Volcano Modelling to Volcano Geology,* pp. 23–53, InTech. doi:10.5772/63959

Cannata, A., Hellweg, M., Grazia, G. Di, Ford, S., Alparone, S., Gresta, S., Montalto, P. & Patanè, D., 2009. Long period and very long period events at Mt. Etna volcano: characteristics, variability and causality, and implications for their sources. *J. Volc. Geotherm. Res.,* **187,** 227–249.

Cauchie, L., Saccorotti, G. & Bean, C.J., 2015. Amplitude and recurrence time analysis of LP activity at Mount Etna, Italy. *J. geophys. Res.: Solid Earth,* **120,** 6474–6486.

Cesca, S., Battaglia, J., Dahm, T., Tessmer, E., Heimann, S. & Okubo, P., 2008. Effects of topography and crustal heterogeneities on the source estimation of LP event at Kilauea volcano. *Geophys. J. Int.,* **172,** 1219–1236.

Cesca, S. & Grigoli, F., 2015. Full waveform seismological advances for microseismic monitoring,in *Advances in Geophysics,* Vol. **56,** pp. 169–228, Elsevier.

Cesca, S., Grigoli, F., Heimann, S., Dahm, T., Kriegerowski, M., Sobiesiak, M., Tassara, C. & Olcay, M., 2016. The M w 8.1 2014 Iquique, Chile, seismic sequence: a tale of foreshocks and aftershocks. *Geophys. J. Int.,* **204,** 1766–1780.

Cesca, S., Şen, A.T. & Dahm, T., 2014. Seismicity monitoring by cluster analysis of moment tensors. *Geophys. J. Int.,* **196,** 1813–1826.

Chouet, B., 1986. Dynamics of a fluid-driven crack in three dimensions by the finite difference method. *J. geophys. Res.,* **91,** 13967.

Chouet, B., 1988. Resonance of a fluid-driven crack: radiation properties and implications for the source of long-period events and harmonic tremor. *J. geophys. Res.,* **93,** 4375–4400.

Chouet, B., 2003. Volcano seismology. *Pure appl. Geophys.,* **160,** 739–788.

Chouet, B.A., 1996. Long-period volcano seismicity: its source and use in eruption forecasting. *Nature,* **380,** 309–316.

Chouet, B.A. & Matoza, R.S., 2013. A multi-decadal view of seismic methods for detecting precursors of magma movement and eruption. *J. Volc. Geotherm. Res.,* **252,** 108–175.

Chouet, B.A., Page, R.A., Stephens, C.D., Lahr, J.C. & Power, J.A., 1994. Precursory swarms of long-period events at Redoubt Volcano (1989–1990), Alaska: their origin and use as a forecasting tool. *J. Volc. Geotherm. Res.,* **62,** 95–135.

Comte, D., Roecker, S.W. & Suárez, G., 1994. Velocity structure in northern Chile: evidence of subducted oceanic crust in the Nazca Plate. *Geophys. J. Int.,* **117,** 625–639.

Cusano, P., Petrosino, S. & Saccorotti, G., 2008. Hydrothermal origin for sustained Long-Period (LP) activity at Campi Flegrei Volcanic Complex, Italy. *J. Volc. Geotherm. Res.,* **177,** 1035–1044.

Del Pezzo, E., Bianco, F. & Borgna, I., 2013. Magnitude scale for LP events: a quantification scheme for volcanic quakes. *Geophys. J. Int.,* **194,** 911–919.

Del Pezzo, E., Godano, C., Gorini, A. & Martini, M., 1992. Wave polarization and location of the source of the explosion quakes at Stromboli Volcano. in *Volcanic Seismology,* Vol. **3,** pp. 279–296, Springer, Berlin, Heidelberg.

Dorbath, C., Gerbault, M., Carlier, G. & Guiraud, M., 2008. Double seismic zone of the Nazca plate in northern Chile: high-resolution velocity structure, petrological implications, and thermomechanical modeling. *Geochem., Geophys. Geosyst.,* **9**.

Dzurisin, D., 2007. *Volcano Deformation – Geodetic Monitoring Techniques,* Springer, Springer-Praxis Books in Geophysical Sciences.

Díaz, D., Brasse, H. & Ticona, F., 2012. Conductivity distribution beneath Lascar volcano (Northern Chile) and the Puna, inferred from magnetotelluric data. *J. Volc. Geotherm. Res.,* **217–218,** 21–29.

Gaete, A., Kavanagh, J.L., Rivalta, E., Hilmi Hazim, S., Walter, T.R. & Dennis, D.J.C., 2019. The impact of unloading stresses on post-caldera magma intrusions. *Earth planet. Sci. Lett.,* **508,** 109–121.

GEOFON Data Centre, 1993. GEOFON Seismic Network. Deutsches GeoForschungsZentrum GFZ, *Other/Seismic Network,* doi:10.14470/TR560404.

Gharti, H.N., Oye, V., Roth, M. & Kühn, D., 2010. Automated microearthquake location using envelope stacking and robust global optimization. *Geophysics,* **75,** MA27–MA46.

Global Volcanism Program, 2013. Volcanoes of the World - Lascar (355100). Smithsonian Institiution, .

Global Volcanism Program, 2016. Report on Lascar (Chile) — July 2016. *Smithson. Inst.,* **41,** 7. Retrieved from http://volcano.si.edu/showreport.cfm?doi=10.5479/si.GVP.BGVN201607-355100

González, C., Inostroza, M., Aguilera, F., González, R., Viramonte, J. & Menzies, A., 2015. Heat and mass flux measurements using Landsat images from the 2000–2004 period, Lascar volcano, northern Chile. *J. Volc. Geotherm. Res.,* **301,** 277–292.

González, D.M., Bataille, K., Eulenfeld, T. & Franco, L.E., 2016. Temporal seismic wave velocity variations at Láscar volcano. *Andean Geol.,* **43,** 240–246.

Grazia, G. Di, Falsaperla, S. & Langer, H., 2006. Volcanic tremor location during the 2004 Mount Etna lava effusion. *Geophys. Res. Lett.,* **33,** L04304.

Gressier, J.-B., Mourgues, R., Bodet, L., Matthieu, J.-Y., Galland, O. & Cobbold, P., 2010. Control of pore fluid pressure on depth of emplacement of magmatic sills: An experimental approach. *Tectonophysics,* **489,** 1–13.

Grigoli, F., Cesca, S., Amoroso, O., Emolo, A., Zollo, A. & Dahm, T., 2014. Automated seismic event location by waveform coherence analysis. *Geophys. J. Int.,* **196,** 1742–1753.

Grigoli, F., Cesca, S., Vassallo, M. & Dahm, T., 2013. Automated seismic event location by travel-time stacking: an application to mining induced seismicity. *Seismol. Res. Lett.,* **84,** 666–677.

Hellweg, M., 2000. Physical models for the source of Lascar's harmonic tremor. *J. Volc. Geotherm. Res.,* **101,** 183–198.

Jurkevics, A., 1988. Polarization analysis of three-component array data. *Bull. seism. Soc. Am.,* **78,** 1725–1743, Seismological Society of America. Retrieved from https://pubs.geoscienceworld.org/ssa/bssa/article/78/5/1725/119105/polarization-analysis-of-three-component-array

Kao, H. & Shan, S.-J., 2004. The Source-Scanning Algorithm: mapping the distribution of seismic sources in time and space. *Geophys. J. Int.,* **157,** 589–594.

Kao, H. & Shan, S.J., 2007. Rapid identification of earthquake rupture plane using Source-Scanning Algorithm. *Geophys. J. Int.,* **168,** 1011–1020.

Kawakatsu, H. & Yamamoto, M., 2015. Volcano seismology,in *Treatise on Geophysics,* Vol. **4,** pp. 389–419, Elsevier.

Kay, S.M. & Coira, B.L., 2009. Shallowing and steepening subduction zones, continental lithospheric loss, magmatism, and crustal flow under the Central Andean Altiplano-Puna Plateau,in *Backbone of the Americas: Shallow Subduction, Plateau Uplift, and Ridge and Terrane Collision,* Vol. **204,** pp. 229–259, Geological Society of America.

Kumagai, H., Placios, P., Ruiz, M., Yepes, H. & Kozono, T., 2011. Ascending seismic source during an explosive eruption at Tungurahua volcano, Ecuador. *Geophys. Res. Lett.,* **38,** L01306.

Lahr, J.C., Chouet, B.A., Stephens, C.D., Power, J.A. & Page, R.A., 1994. Earthquake classification, location, and error analysis in a volcanic environment: implications for the magmatic system of the 1989–1990 eruptions at redoubt volcano, Alaska. *J. Volc. Geotherm. Res.,* **62,** 137–151.

Latter, J.H., 1981. Volcanic earthquakes, and their relationship to eruptions at Ruapehu and Ngauruhoe volcanoes. *J. Volc. Geotherm. Res.,* **9,** 293–309.

Lee, W. & Lahr, J., 1972. HYPO71 : a computer program for determining hypocenter, magnitude, and first motion pattern of local earthquakes, U.S. Geol. Surv. Open-File Rept. 75, doi:10.3133/OFR72224.

Lokmer, I., Saccorotti, G., Lieto, B. Di & Bean, C.J., 2008. Temporal evolution of long-period seismicity at Etna Volcano, Italy, and its relationships with the 2004–2005 eruption. *Earth planet. Sci. Lett.,* **266,** 205–220.

Maccaferri, F., Bonafede, M. & Rivalta, E., 2011. A quantitative study of the mechanisms governing dike propagation, dike arrest and sill formation. *J. Volc. Geotherm. Res.,* **208,** 39–50.

Marchetti, E. & Ripepe, M., 2005. Stability of the seismic source during effusive and explosive activity at Stromboli Volcano. *Geophys. Res. Lett.,* **32,** L03307.

Matoza, R.S., Shearer, P.M., Lin, G., Wolfe, C.J. & Okubo, P.G., 2013. Systematic relocation of seismicity on Hawaii Island from 1992 to 2009 using waveform cross correlation and cluster analysis. *J. geophys. Res.: Solid Earth,* **118,** 2275–2288.

Matoza, R.S., Shearer, P.M. & Okubo, P.G., 2014. High-precision relocation of long-period events beneath the summit region of Kīlauea Volcano, Hawai'i, from 1986 to 2009. *Geophys. Res. Lett.,* **41,** 3413–3421.

Matthews, S.J., Gardeweg, M.C. & Sparks, R.S.J., 1997. The 1984 to 1996 cyclic activity of Lascar Volcano, northern Chile: Cycles of dome growth, dome subsidence, degassing and explosive eruptions. *Bull. Volcanol.,* **59,** 72–82.

McNutt, S.R., 2005. Volcanic Seismology. *Annu. Rev. Earth planet. Sci.,* **33,** 461–491.

Montalbetti, J.F. & Kanasewich, E.R., 1970. Enhancement of teleseismic body phases with a polarization filter. *Geophys. J. R. astr. Soc.,* **21,** 119–129.

Morioka, H., Kumagai, H. & Maeda, T., 2017. Theoretical basis of the amplitude source location method for volcano-seismic signals. *J. geophys. Res.: Solid Earth,* **122,** 6538–6551.

Nakano, M. & Kumagai, H., 2005. Waveform inversion of volcano-seismic signals assuming possible source geometries. *Geophys. Res. Lett.,* **32,** n/a-n/a, doi:10.1029/2005GL022666

Neuberg, J. & Luckett, R., 1996. Seismo-volcanic sources on Stromboli volcano. *Ann. Di Geofis.* doi:10.4401/ag-3969.

Neuberg, J., Luckett, R., Ripepe, M. & Braun, T., 1994. Highlights from a seismic broadband array on Stromboli Volcano. *Geophys. Res. Lett.,* **21,** 749–752.

Neuberg, J. & Pointer, T., 2000. Effects of volcano topography on seismic broad-band waveforms. *Geophys. J. Int.,* **143,** 239–248.

Neuberg, J.W., Tuffen, H., Collier, L., Green, D., Powell, T. & Dingwell, D., 2006. The trigger mechanism of low-frequency earthquakes on Montserrat. *J. Volc. Geotherm. Res.,* **153,** 37–50.

Ovdas, O.V. de los A. del S., 2013. *Reporte Especial de Actividad Volcánica - Región de Antofagasta,* Temuco.

Ovdas, O.V. de los A. del S., 2015. *Reporte de Actividad Volcánica (RAV) - Región de Antofagasta,* Temuco.

Patanè, D., Grazia, G. Di, Cannata, A., Montalto, P. & Boschi, E., 2008. Shallow magma pathway geometry at Mt. Etna volcano. *Geochem., Geophys. Geosyst.,* **9**.

Pavez, A. *et al.*, 2006. Insight into ground deformations at Lascar volcano (Chile) from SAR interferometry, photogrammetry and GPS data: implications on volcano dynamics and future space monitoring. *Remote Sens. Environ.,* **100,** 307–320.

Petersen, T., Caplan-Auerbach, J. & McNutt, S.R., 2006. Sustained long-period seismicity at Shishaldin Volcano, Alaska. *J. Volc. Geotherm. Res.,* **151,** 365–381.

Prejean, S., Stork, A., Ellsworth, W., Hill, D. & Julian, B., 2003. High precision earthquake locations reveal seismogenic structure beneath Mammoth Mountain, California. *Geophys. Res. Lett.,* **30**.

Pritchard, M.E. & Simons, M., 2002. A satellite geodetic survey of large-scale deformation of volcanic centres in the central Andes. *Nature,* **418,** 167–171.

Richter, N., Salzer, J.T., Zeeuw-van Dalfsen, E. de, Perissin, D. & Walter, T.R., 2018. Constraints on the geomorphological evolution of the nested summit craters of Láscar volcano from high spatio-temporal resolution TerraSAR-X interferometry. *Bull. Volcanol.,* **80,** 21.

Roman, D.C. & Gardine, M.D., 2013. Seismological evidence for long-term and rapidly accelerating magma pressurization preceding the 2009 eruption of Redoubt Volcano, Alaska. *Earth planet. Sci. Lett.,* **371–372,** 226–234.

Saccorotti, G., Lokmer, I., Bean, C.J., Grazia, G. Di & Patanè, D., 2007. Analysis of sustained long-period activity at Etna Volcano, Italy. *J. Volc. Geotherm. Res.,* **160,** 340–354.

Schaff, D.P. & Waldhauser, F., 2005. Waveform cross-correlation-based differential travel-time measurements at the northern California seismic network. *Bull. seism. Soc. Am.,* **95,** 2446–2461.

Silva, S.L. de, 1989. Altiplano-Puna volcanic complex of the central Andes. *Geology,* **17,** 1102.

Taisne, B., Brenguier, F., Shapiro, N.M. & Ferrazzini, V., 2011. Imaging the dynamics of magma propagation using radiated seismic intensity. *Geophys. Res. Lett.,* **38,** L04304.

Tassi, F., Aguilera, F., Vaselli, O., Medina, E., Tedesco, D., Delgado Huertas, A., Poreda, R. & Kojima, S., 2009. The magmatic- and hydrothermal-dominated fumarolic system at the Active Crater of Lascar volcano, northern Chile. *Bull. Volcanol.,* **71,** 171–183.

Waldhauser, F., 2001. HypoDD: A computer program to compute double-difference hypocenter locations. U.S. Geol. Surv. Open-File Rept. Retrieved from http://core.ac.uk/download/pdf/27299001.pdf.

Waldhauser, F. & Ellsworth, W.L., 2000. A Double-difference Earthquake location algorithm: Method and application to the Northern Hayward Fault, California. *Bull. seism. Soc. Am.,* **90,** 1353–1368.

Wassermann, J., 2012. Volcano Seismology. in *New Manual of Seismological Observatory Practice 2 (NMSOP-2),* Vol. **1,** pp. 1–67, Deutsches GeoForschungsZentrum GFZ. doi:10.2312/GFZ.NMSOP-2_ch13

Wegler, U. & Lühr, B.-G., 2001. Scattering behaviour at Merapi volcano (Java) revealed from an active seismic experiment. *Geophys. J. Int.,* **145,** 579–592.

Whelley, P.L., Jay, J., Calder, E.S., Pritchard, M.E., Cassidy, N.J., Alcaraz, S. & Pavez, A., 2012. Post-depositional fracturing and subsidence of pumice flow deposits: Lascar Volcano, Chile. *Bull. Volcanol.,* **74,** 511–531.

Wooster, M.J., 2001. Long-term infrared surveillance of Lascar Volcano: Contrasting activity cycles and cooling pyroclastics. *Geophys. Res. Lett.,* **28,** 847–850.

Zeeuw-van Dalfsen, E. de, Richter, N., González, G. & Walter, T.R., 2017. Geomorphology and structural development of the nested summit crater of Láscar Volcano studied with Terrestrial Laser Scanner data and analogue modelling. *J. Volc. Geotherm. Res.,* **329,** 1–12.

Zeng, X., Zhang, H., Zhang, X., Wang, H., Zhang, Y. & Liu, Q., 2014. Surface microseismic monitoring of hydraulic fracturing of a shale-gas reservoir using short-period and broadband seismic sensors. *Seismol. Res. Lett.,* **85,** 668–677.

Zobin, V., 2012. *Introduction to Volcanic Seismology,* Elsevier.